PHOTONICS Research

Tailoring directional chiral emission from molecules coupled to extrinsic chiral quasi-bound states in the continuum

Minpeng Liang,[1,7] Lucio Claudio Andreani,[2,8] Anton Matthijs Berghuis,[1] José Luis Pura,[3,4] Shunsuke Murai,[5] Hongguang Dong,[1,6] José A. Sánchez-Gil,[3] and Jaime Gómez Rivas[1,*]

[1]Department of Applied Physics and Science Education, Institute for Complex Molecular Systems, and Eindhoven Hendrik Casimir Institute, Eindhoven, 5600 MB, The Netherlands
[2]Dipartimento di Fisica, Università di Pavia, 27100 Pavia, Italy
[3]Instituto de Estructura de la Materia (IEM), Consejo Superior de Investigaciones Científicas, 28006 Madrid, Spain
[4]GdS-Optronlab, Física de la Materia Condensada, Universidad de Valladolid, 47011 Valladolid, Spain
[5]Department of Material Chemistry, Graduate School of Engineering, Kyoto University, Kyoto 615-8510, Japan
[6]Centre for Optical and Electromagnetic Research, National Engineering Research Center for Optical Instruments, Zhejiang University, Hangzhou 310027, China
[7]e-mail: lmpmse@163.com
[8]e-mail: lucio.andreani@unipv.it
*Corresponding author: J.Gomez.Rivas@tue.nl

Received 3 May 2024; revised 4 August 2024; accepted 15 August 2024; posted 16 August 2024 (Doc. ID 528976); published 11 October 2024

We investigate the chiral emission from non-chiral molecules coupled to metasurfaces with a unit cell formed by dimers of detuned and displaced Si nanodisks. The detuning and displacement lead to the formation of narrow modes, known as quasi-bound states in the continuum (Q-BICs), with different electric and magnetic characteristics. The dispersion and character of the modes are explained by using the guided-mode expansion method and finite-element simulations. The coupling between these modes leads to an extrinsic chiral response with large circular dichroism for defined energies and wavevectors. When the lattice constant of the metasurface is changed, the dispersion of the extrinsic chiral Q-BICs can be tuned and the emission properties of a thin film of dye molecules on top of the metasurface are modified. In particular, we observe strongly directional and circularly polarized emission from the achiral dye molecules with a degree of circular polarization reaching 0.8 at the wavelengths defined by the dispersion of the Q-BICs. These results could enable the realization of compact light sources with a large degree of circular polarization for applications in displays, optical recording, or optical communication.

https://doi.org/10.1364/PRJ.528976

1. INTRODUCTION

Chirality refers to the property of asymmetric objects, by which they cannot be superimposed on their mirror image with translations and rotations. This property is widespread in nature, with important consequences in very different areas, such as chemistry, biology, or photonics [1]. Well-known examples of structures that exhibit inherent chirality include proteins, sugars, or DNA sequences. A chiral molecule (enantiomer) can be a poison, while its mirror enantiomer can act as a medicine, even though both molecules have the same chemical composition. Due to several reasons, such as random orientation, interaction with the environment, and the influence of thermal motion, most natural materials exhibit weak intrinsic chiral responses, which limits their application in, e.g., displays, optical recording, or optical communication. To overcome these limitations and explore more possibilities for chiral materials, controlling the chiral response of natural materials becomes crucial. One approach to achieve this control in optics/photonics is by coupling photonic or plasmonic metasurfaces with strong chiral responses and supporting modes with high quality factors (Q-factors) and large electric field (E-field) enhancements, such as surface lattice resonances [2–13], to weakly chiral or even non-chiral emitters [14–23].

Particularly interesting are bound states in the continuum (BICs), which are optical modes with infinite lifetimes and Q-factors that originate from destructive interference of radiative channels or from the symmetry of the electromagnetic field. These modes remain localized to the structure even though they coexist with the continuum of radiative modes, since they cannot couple to this continuum [24]. BICs offer

many promising possibilities to modify light–matter interactions due to their divergent Q-factor and the strong enhancement of the E-field [25–27]. In particular, symmetry-protected BICs in periodic two-dimensional metasurfaces with inversion symmetry have recently been proposed and investigated, both fundamentally and in relation to applications [26,28–30]. By slightly breaking the inversion symmetry of the metasurface, BICs evolve into quasi-BICs (Q-BICs), with finite but still very large Q-factors and strong E-field enhancements. In addition, if the structure with broken inversion symmetry is mirror asymmetric, it will also introduce optical chirality, resulting in chiral Q-BICs [31,32].

Intrinsic chiral BICs (chiral structures for light incident in the normal direction) with large optical dichroism are difficult to achieve experimentally, as they require breaking the out-of-plane symmetry [33,34]. However, it is relatively easy to obtain intrinsic and extrinsic chiral Q-BICs (chiral at an oblique angle) only by breaking the symmetry in the plane [35,36], which extends the applications of chiral Q-BICs [37–39]. Recent studies show that chiral emission can be achieved through chiral Q-BICs [40–42]. However, to the best of our knowledge, studies on directional chiral emission based on chiral Q-BICs have not yet been reported. Directional and polarized emission from metasurfaces will have an impact in different application areas, such as communication systems, imaging systems, radar/laser systems, and light-emitting diodes [43–48].

Motivated by these recent advances, we present here an investigation of the directional chiral emission from achiral molecules coupled to extrinsic chiral Q-BICs in a silicon metasurface. We choose achiral molecules to be able to attribute any change in their polarized emission to the effect of the metasurface. The metasurface is formed by dimers of Si nanodisks. Detuning of geometric parameters, including diameters and relative distances between nanodisks, is used to break the inversion symmetry of the metasurface and introduce optical chirality, resulting in four extrinsic chiral Q-BICs in the visible range. The nature of the chiral Q-BICs was confirmed and investigated experimentally and theoretically by the circular dichroism of the optical extinction. The directional emission of achiral dye molecules coupled to extrinsic chiral Q-BICs has also been explored, showing several directional chiral emitting modes emerging from the dispersion of the lattice. With our design of symmetry-broken metasurface, we demonstrate a very large degree of circular polarization (DCP as high as 0.8) in defined directions. In addition, there is an up to 13-fold enhancement of the photoluminescence due to the coupling of the emission to the array and the subsequent decoupling of polarized emission in defined directions. The directionality is controlled by the lattice constant, and the divergence angle of the far-field directional chiral emission is extremely small (∼2 deg). These results demonstrate the possibility of achieving strongly chiral Q-BIC emission with good control of directionality and promising perspectives for applications in chiral optical devices.

2. SAMPLE DESIGN

The investigated metasurface consists of an array with a unit cell formed by Si nanodisk dimers. To break the inversion symmetry of the metasurface and open a radiation channel for the BIC, which evolves into a Q-BIC, size and position perturbations to one of the disks of the dimer have been introduced. These perturbations also introduce extrinsic chirality, since they break the in-plane mirror symmetry. The perturbations [illustrated in Fig. 1(a)] are quantified by the parameters $\alpha_{\text{size}} = \Delta r/r$ and $\alpha_{\text{position}} = \Delta x/x$, which describe the normalized difference in radius (r) between the two disks and the relative displacement of the two disks relative to the middle of the unit cell (x). To tune the wavelength of the resonances, samples with different parameters have been prepared. More detailed information on these parameters can be found in Table 1. We selected Si as the material for the metasurface because of its substantial refractive index and low loss within the investigated wavelength range.

A metasurface with a size of 2 mm × 2 mm was patterned on a 90 nm thick polycrystalline Si on a SiO_2 substrate using electron beam lithography and a lift-off process (see Appendix A) [49]. Figure 1(b) shows a scanning electron microscope (SEM) image of the metasurface. The top panel of Fig. 1(c) illustrates a unit cell of the metasurface, indicating the different geometric parameters. A polymethyl methacrylate (PMMA)/dye solution (25% (mass fraction) perylene dye [N,N'-bis(2,6-diisopropylphenyl)-1,7- and -1,6-bis(2,6-diisopropylphenoxy)-perylene-3,4:9,10-tetracarboximide] in PMMA) was spin-coated on top of the metasurface, forming a layer with a thickness of ≈200 nm, as illustrated in the bottom panel of Fig. 1(c). Figure 1(d) shows the normalized photoluminescence (PL) spectrum (red curve) and the normalized extinction (1-transmission) (blue curve) of a layer of PMMA/dye molecules. Two peaks are visible in the extinction, corresponding to the electronic transition at 2.24 eV and its first vibronic replica

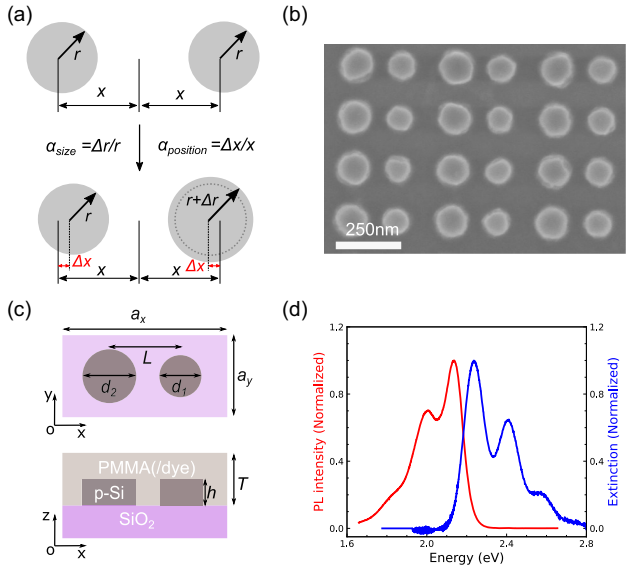

Fig. 1. (a) Illustration of a unit cell of the metasurface with the geometric parameters and asymmetry parameters. (b) SEM image (top view) of a representative Si metasurface on a SiO_2 substrate (without PMMA/dye). (c) The top panel represents the top view of one unit cell of the metasurface, and the bottom panel is the side view of the sample structure. (d) Normalized PL emission (red) and extinction (1-transmission) (blue) of a layer of dye molecules in PMMA.

Table 1. Geometric Parameters of the Investigated Samples, Labeled as S0 to S5[a]

Samples	d_1 (nm)	d_2 (nm)	L (nm)	a_x (nm)	a_y (nm)	α_{size}	$\alpha_{position}$
S0	100	126	165	383	193	0.230	0.138
S1	98	122	172	383	197	0.245	0.102
S2	108	135	183	400	203	0.250	0.185
S3	110	138	192	422	208	0.254	0.198
S4	118	146	200	443	218	0.237	0.215
S5	120	150	207	458	232	0.250	0.246

[a]d_1, d_2, L, a_x, a_y, α_{size}, and $\alpha_{position}$ are measured from SEM images. α_{size} and $\alpha_{position}$ are the size and position asymmetry parameters, respectively.

at 2.41 eV, respectively. Similarly, there are also two excitonic peaks (at 2.00 and 2.14 eV) in the PL spectrum.

We notice that PMMA is transparent in the visible and it matches the refractive index of the substrate, yielding a structure with almost perfect xy mirror symmetry, which is the best condition to reduce unwanted radiative losses. Since the dye's absorption affects the metasurface extinction, we have first studied the optical properties of the bare photonic modes in the metasurface with PMMA alone, before describing the combination of the metasurface with PMMA/dye. The thickness of the PMMA/dye layer is critical, as the interaction of the dye with the optical modes should be significant, while the dye absorption should not mask the contribution from the photonic modes: the chosen thickness $T = 200$ nm follows from a trade-off between these two criteria.

3. OPTICAL EXTINCTION OF CIRCULARLY POLARIZED LIGHT AND CIRCULAR DICHROISM

To investigate the chiral response of the bare metasurface, we measured and simulated the dispersion of the extinction of circularly polarized light. A layer of PMMA without dye molecules was spin-coated on top of the array to match the refractive index of the SiO_2 substrate. Figures 2(a) and 2(b) show the experimental extinction spectra as a function of the incident wavevector (k_y) parallel to the surface of the array with right-handed circularly polarized (RCP) and left-handed circularly polarized (LCP) white light, respectively. k_y is given by $k_y = (2\pi/\lambda)\sin\theta$, where λ is the wavelength and θ is the incident angle in the yz plane. The experimental setup is described in Appendix A. Four distinct modes, labeled M1 to M4, are visible in the extinction measurements. The RCP extinction decreases substantially for the M1 and M4 modes, along with the increase of the parallel wavevector from −8 to 8 rad/μm, limited by the numerical aperture of the objective [Fig. 2(a)]. In contrast, the extinction of the M2 and M3 modes increases from 0 to 0.35 when the wavevector increases from −8 to 8 rad/μm. For the extinction of LCP light [Fig. 2(b)], the modes share the same trend as the mirror image of Fig. 2(a). We notice that some of the modes (most notably M3) are spectrally narrow close to $k = 0$. The reason for this narrowing is that they originate from BICs in the size-detuned structure. M4 is considerably broader because it is an electric dipole mode (p_y) and is radiative even for the size-detuned structure. Figure 2(c) shows the circular dichroism (CD) of extinction, given by

$$\mathrm{CD} = \frac{\mathrm{LCP} - \mathrm{RCP}}{\mathrm{LCP} + \mathrm{RCP}}. \tag{1}$$

At the Γ point ($k_y = 0$), the CD of all modes is zero. Upon increasing k_y, the absolute value of the CD of all modes increases. The integrated CD over positive and negative wavevectors is zero, indicating that the metasurface is not intrinsically chiral as can be also deduced from the symmetry.

Simulations of the optical properties were performed using a Bloch-mode scattering matrix method with the software EMUstack [50,51], which yields a solution of Maxwell equations for field propagation in layered media. The structural parameters of the simulated metasurface are those from sample S0. The refractive indices of Si and SiO_2 were taken from Ref. [52], and the refractive index of PMMA is considered constant with a value of 1.49. The results of the simulations are shown in Figs. 2(d) and 2(e) for RCP and LCP light, respectively. Figure 2(f) shows the calculated CD in extinction. The simulated results are in excellent agreement with the experiments concerning the dispersion and the intensity of the four modes for the two circular polarizations. In particular, we see that in each of the two wavevector directions, two modes have positive CD while the other two have negative CD. Such features can be understood by the analytic model based on symmetry, as discussed in the next section.

4. MODE DISPERSION AND NEAR-FIELD DISTRIBUTION

We consider the metasurface described in Fig. 1(b), with the unit cell in the upper panel of Fig. 1(c). In the approximation of a 2D structure with an effective refractive index n_{eff}, the dispersion of photonic modes can be expressed by taking into account diffraction by the lowest-order reciprocal lattice vectors as

$$\omega_{\pm}(k) = \frac{c}{n_{\mathrm{eff}}}\sqrt{\left(k_x + m\frac{2\pi}{a_x}\right)^2 + k_y^2}, \quad m = \pm 1. \tag{2}$$

There are two pairs of such modes, xy-even and xy-odd, which in principle may have a different effective index n_{eff}. The modes are degenerate at $k = 0$, but this degeneracy is removed by the periodic structure of the metasurface. To get a better description of the photonic dispersion, we show in Fig. 3 the dispersion of photonic modes in the symmetry-broken metasurface of Fig. 1(b), calculated by the guided-mode expansion method [53–55]. Notice that xy-even modes are often

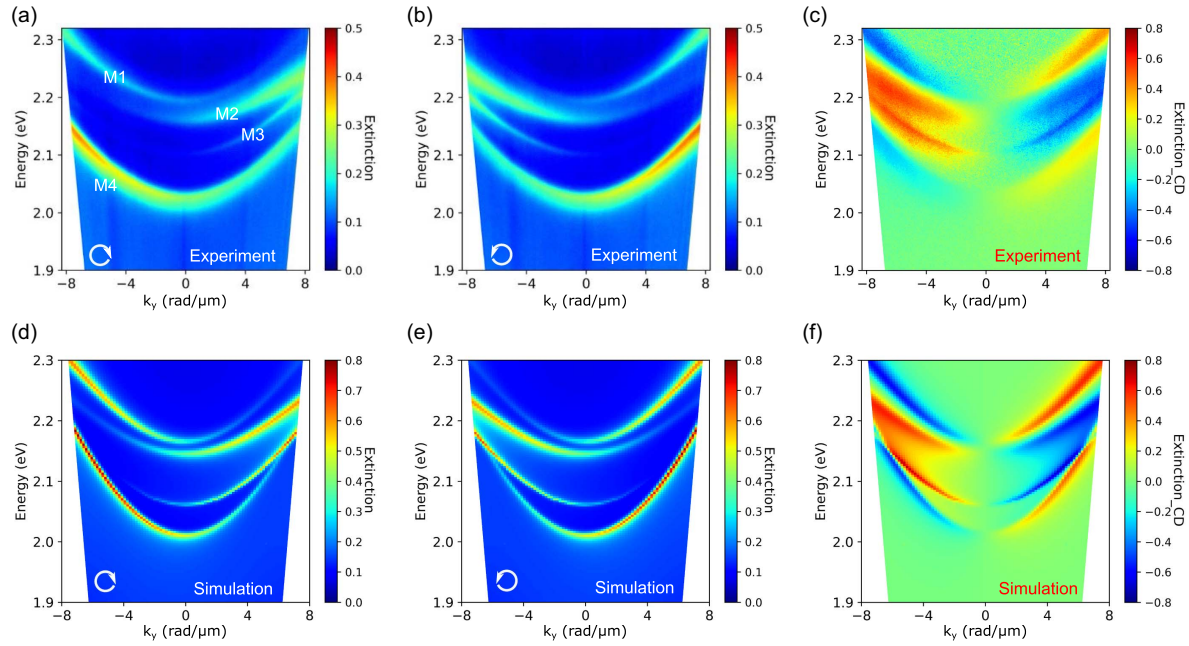

Fig. 2. Measured and simulated extinction circular dichroism of metasurface S0 with a ∼300 nm thick PMMA layer on top. (a), (b) Measured extinction spectra as a function of the incident wavevector parallel to the surface of the metasurface for right-handed and left-handed circularly polarized light, respectively. The four distinct modes observed in the extinction measurements are indicated in (a). (c) Experimental dispersion of the circular dichroism. (d), (e) Simulated extinction dispersion for right-handed and left-handed circularly polarized light, respectively. (f) Simulated dispersion of the circular dichroism.

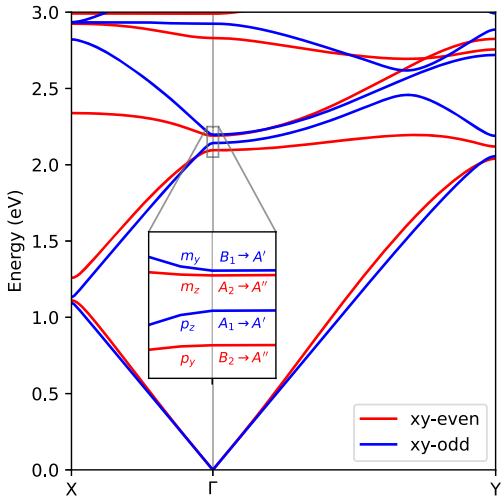

Fig. 3. Dispersion of photonic modes in the investigated metasurface, calculated with the guided-mode expansion. The symmetry points in the 2D Brillouin zone are $\Gamma = (0, 0)$, $X = (\frac{2\pi}{a_x}, 0)$, $Y = (0, \frac{2\pi}{a_y})$. The inset shows a zoom of the region around $k = 0$, with the dominant dipolar character of the modes and the symmetry labels explained in Appendix B.

called TE-like in photonic crystal terminology, while *xy*-odd modes are often called TM-like: see Ref. [55] for a full discussion of polarization properties. At the Γ-point, there are four modes between 2 and 2.3 eV, which result from diffraction by the wavevectors $\mathbf{G} = (\pm G, 0)$ along the x direction. As shown by the group-theory treatment in Appendix B, these four modes, in order of increasing energy, have symmetries of electric and magnetic dipole moments along the y and z directions, p_y, p_z, m_z, m_y, as indicated in the inset. The dispersion along the Γ-X direction was investigated in Ref. [49] for TE polarization, which probes the *xy*-even modes. The dispersion along Γ-Y can be compared with the results of Section 3, with the modes m_y, m_z, p_z, p_y corresponding to the modes M1, M2, M3, M4 in Fig. 2.

The different characteristics of the modes can be more easily revealed through the near-field distributions of the electric field. The metasurface is numerically studied with COMSOL Multiphysics. The solution, shown in Fig. 4, provides the Bloch eigenmodes of the infinite metasurface at $k = 0$. Modes dominated by the electric dipole moments along the y and z directions, p_y and p_z, are characterized by a parallel electric field inside the Si disks along the y and z axes, respectively. On the other hand, magnetic-like modes, m_y and m_z, appear as a curl of the electric field around the y and z axes, respectively, similar to point-like magnetic dipoles. The symmetries of the field distributions exactly satisfy the symmetry conditions stated in Table 2 in Appendix B, presenting either symmetry (*xy*-odd modes) or anti-symmetry (*xy*-even modes) with respect to the *xz* plane.

From this analysis, we can derive the main chiral properties of the photonic modes and compare them with those of the experiments. At any wavevector $k_y \neq 0$, all mirror symmetries are broken and the properties of the metasurface become

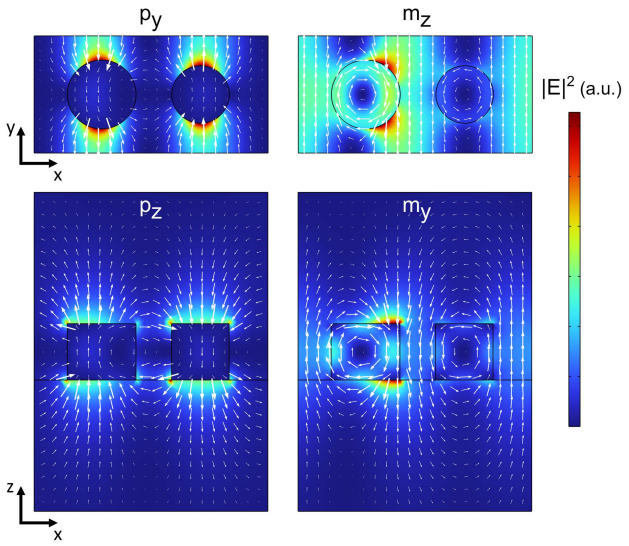

Fig. 4. Near-field distribution of the electric field for the four studied modes, numerically calculated with COMSOL. The color scale represents the magnitude of the electric field, $|E|^2$, and the arrows represent the electric field direction and magnitude. The projection planes, *xy* and *xz*, are chosen to better illustrate the character of each mode: *xy*-even modes are plotted on the *xy* plane, while *xy*-odd modes are projected onto the *xz* plane, in both cases containing the centers of both disks.

extrinsically chiral. Indeed, at any $k_y \neq 0$ the p_y and m_z modes are coupled together, as are the p_z, m_y modes. We can relate the chiral optical response to the far-field polarization vector and the Stokes parameter S_3, following the approach of Ref. [56]. A non-zero Stokes parameter S_3 indicates a finite ellipticity of the eigenmodes, which results in a circular dichroism. The detailed analysis is reported in Appendix B, and only the main results are summarized here. Basically, the two coupled p_y and m_z modes give rise to two chiral eigenmodes with opposite ellipticity, and the same applies for the two coupled p_z, m_y modes. Thus, for any wavevector $k_y > 0$, we expect that two of the four eigenmodes display positive CD, while the other two have negative CD. In addition, the eigenmodes for $k_y < 0$ can be obtained from the corresponding eigenmodes for $k_y > 0$ by mirror reflection, which reverses the ellipticity and the resulting CD in extinction and photoluminescence, i.e., $\mathrm{CD}(-\theta) = -\mathrm{CD}(\theta)$. Thus, we can explain the main features observed in the experiments and the numerical simulations.

5. CHIRAL DISPERSION AND DIRECTIONAL EMISSION MEASUREMENTS

To investigate the chiral emission of the achiral dye molecules coupled to the different modes, and to understand the tunability of the chirality in emission, the achiral dye mixed with PMMA ($n = 1.59$, $T \approx 200$ nm) has been spin-coated at the top of the metasurface. Figures 5(a) and 5(b) show the dispersion of the PL from the bare dye layer on the substrate (off the metasurface) for right-handed (RCPL) and left-handed (LCPL) circularly polarized emission, respectively. A description of how the measurements have been performed can be found in Appendix A. The non-dispersive emission band at around 2.16 eV corresponds to direct exciton emission. There is almost no difference in the intensity of the PL between the RCPL and the LCPL, as can be seen in the degree of circular polarization of the photoluminescence (DCP), shown in Fig. 5(c) and defined as

$$\mathrm{DCP} = \frac{\mathrm{LCPL} - \mathrm{RCPL}}{\mathrm{LCPL} + \mathrm{RCPL}}. \tag{3}$$

The absence of DCP for all wavevectors confirms the achiral nature of the dye. The results are quite different for the emission of the dye on top of the metasurface, as shown in Figs. 5(d) and 5(e) for RCPL and LCPL, respectively. The PL spectra exhibit a pronounced dispersion and a strong chiral response, similar to the extinction of the bare metasurface shown in Fig. 2. Therefore, the emission depends mainly on the chiral properties of the metasurface. Note that the M1 mode in Figs. 5(d) and 5(e) is missing compared to the extinction of the bare metasurface. The reason why M1 is not visible in the PL spectra is that the energy of this mode is higher than the emission range of the dye. Figure 5(f) shows the DCP of the dye on top of the metasurface. Similarly to the CD of the extinction of the bare metasurface, the DCP at the Γ point is 0. The value of the DCP increases along with the increase of the modulus of k_y, reaching its maximum (0.5) for k_y around ±7 rad/μm. Since the nature of the M4 mode is different from that of M2 and M3, the CD of the modes shows the opposite sign when k_y is negative or positive.

To tune the dispersion of the chiral emission, different metasurfaces (S1–S5) with varying geometric parameters, including diameters, periods, and asymmetry parameters, were prepared. The geometric parameters of all samples are listed in Table 1, where S0 refers to the previously described sample (Fig. 5). The DCP of the metasurfaces is presented in Fig. 6. An increase in period and diameter leads to the redshift of the Q-BIC modes [Figs. 6(a)–6(e)], in agreement with Eq. (2). Similarly to S0, S1 to S5 exhibit extrinsic chirality. When $k_y = 0$, the DCP is 0 and increases with the modulus of k_y. The DCP reaches its maximum when k_y is close to ±5.5 rad/μm. The size asymmetry parameter, which defines the normalized difference in radius between nanodisks ($\alpha_{\mathrm{size}} = \Delta r/r$), remains nearly constant at around 0.25 from S1 to S5 (see Table 1). In contrast, the position asymmetry parameter, defined as $\alpha_{\mathrm{position}} = \Delta x/x$, where x denotes the distance from the middle of the unit cell, increases from 0.102 to 0.246. This increase enhances the DCP from S1 to S5. The maximum absolute value of DCP is approximately 0.8 for S5 when k_y is around ±5.46 rad/μm.

The dispersive nature of extrinsic chiral modes leads to directional chiral optical sources. To visualize this directional emission more effectively, polar plots of the emission at 620 ± 10 nm (2 eV) are presented in Fig. 7. For S1 [Fig. 7(a)], the modes are at higher energies and the PL intensity peaks at 0°, leading to similar RCPL and LCPL emissions. As the diameters of the nanodisks and periods of the metasurfaces increase (S2 to S5), the modes redshift, reaching the 620 nm wavelength and revealing the directional chiral emission [Figs. 7(b)–7(e)].

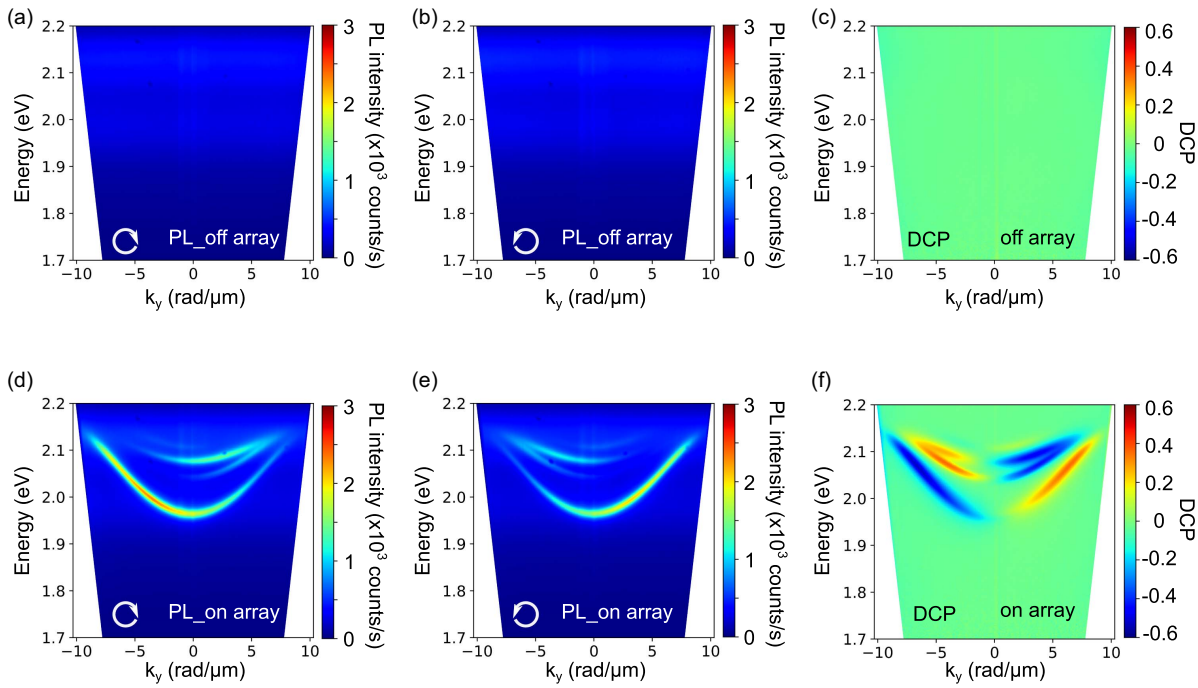

Fig. 5. Measured circular dichroism in the emission of dye coupled to metasurfaces. (a), (b) Experimental dispersion of the PL emission for right- and left-handed circularly polarized light from a PMMA/dye (25% dye, in mass fraction) layer with a thickness of ≈200 nm on top of a substrate. (c) DCP of the PL emitted from this layer. (d), (e) Experimental dispersion of the right- and left-handed circularly polarized PL emission from a PMMA/dye layer on top of the metasurface. (f) DCP of the PL emitted from this layer.

Figure 7 also illustrates that the ideal angle for chiral emission ranges from 30° to 60°, with a divergence as low as 2°. Simulations of directional emission are discussed in Appendix E. The richness of modes in Si metasurfaces makes multidirectional chiral emission feasible and motivates further exploration for potential applications.

We emphasize that the coupling mechanism leading to the directional chiral emission is the spontaneous decay of the excited dye molecules spatially located in the near field of the metasurface, as illustrated in Fig. 4. The molecules decay to the modes supported by the metasurface and these modes leak to the continuum outcoupling the chiral emission due

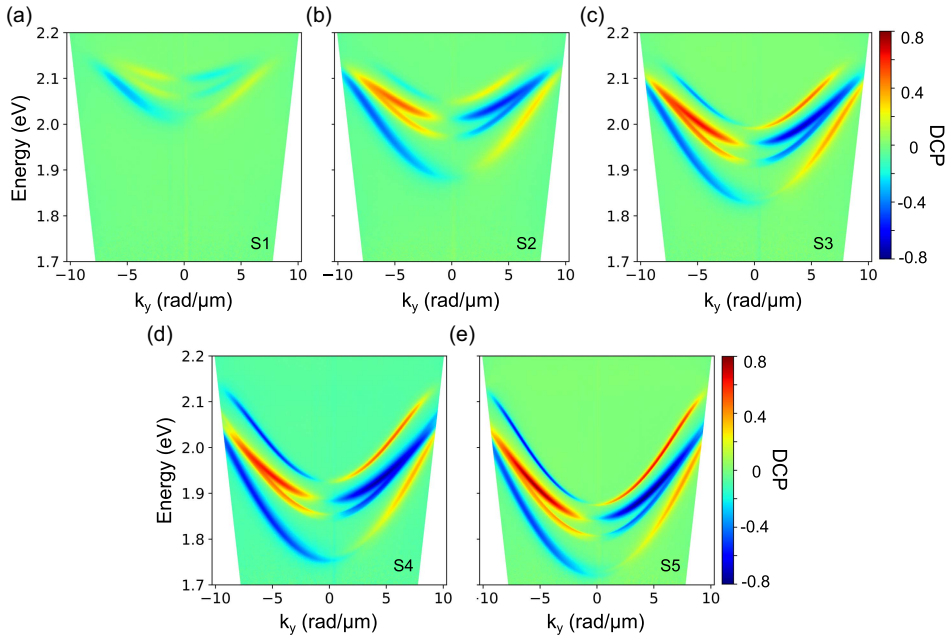

Fig. 6. (a)–(e) Experimental dispersion of the DCP from the metasurfaces S1 to S5 covered with the PMMA/dye film. Along with the increase of size, distance, and lattice from S1 to S5, the position asymmetry parameter increases but the size asymmetry parameter is nearly constant.

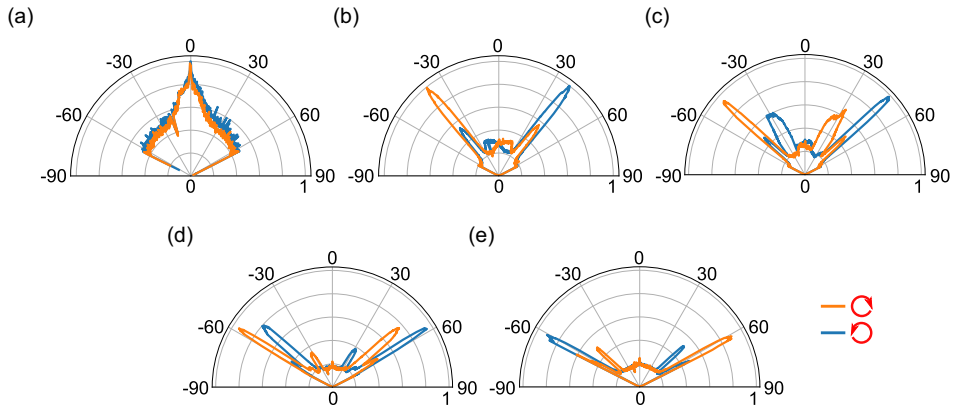

Fig. 7. Experimental RCPL (orange curves) and LCPL (blue curves) intensities at a wavelength of 620 ± 10 nm as a function of the emission angle along y for metasurfaces S1 (a), S2 (b), S3 (c), S4 (d), and S5 (e).

to the broken symmetries discussed in Section 4. Due to the dispersion introduced by the metasurface, the emission outcoupling is highly directional. Although the emission from the molecules is non-chiral, the decay of the emission to a chiral optical mode and subsequent leak of this mode produce a strongly chiral signal. Thus, the symmetry-broken metasurface has a crucial role in producing a strongly directional chiral emission.

6. CONCLUSIONS

In summary, we have demonstrated the chiral directional emission of achiral molecules coupled to metasurfaces formed by asymmetric Si nanodisk dimers. Narrow and dispersive quasi-BICs are supported by the metasurface. The origin of the chiral response of the metasurface and the symmetries of the different optical modes are explained with the guided-mode expansion method and are supported by finite-element numerical simulations. These symmetries are responsible for the large modification of the spectrum, polarization, and direction of emission of the molecules. A large emission enhancement, up to 13 times (shown in Appendix D) over a wide angular range, a small divergence (≃2°), and a DCP as high as 0.8 have been reached. Our study yields a thorough understanding of extrinsic chirality in the investigated metasurfaces, and the results are promising for applications to optical devices that take advantage of strong chiral and directional emission.

APPENDIX A: METHODS

1. Sample Fabrication Method

The metasurface was fabricated as follows. Polycrystalline Si thin films, 90 nm thick, were deposited on a synthetic silica glass substrate using low-pressure chemical vapor deposition with SiH_4 gas as the Si source. A resist (NEB22A2, Sumitomo) was applied to the Si film and subjected to electron-beam lithography. Subsequently, nanodisk arrays of resist were formed on the Si film through development. The Si film was vertically etched via a selective dry etching process (Bosch process), employing SF_6 and C_4F_8 gases, while the resist residue was removed by dry oxygen etching. The resulting array covered an area of 2 mm × 2 mm.

2. Angle-Dependent Extinction Measurements

Angle-dependent extinction was measured using a Fourier microscope, as illustrated in Fig. 8(a). The sample was illuminated with white light (SLS205 xenon lamp, Thorlabs) through a 40× objective lens (Nikon CFI S Plan Fluor ELWD, NA = 0.6) and collected using a 60× objective lens (Nikon CFI S Plan Fluor ELWD, NA = 0.7). The polarization of the incident light could be adjusted by the relative angle orientation of a linear polarizer (LP1) and a quarter-wave plate (QWP1). The fast axis of QWP1 was fixed horizontally to 0°, and circularly polarized light could be achieved by rotating LP1 to ±45°. A similar experimental configuration has been used in recent works to retrieve the DCP from different types of metasurfaces 33,40,41]]. A spectrometer (Princeton Instruments SP2300) connected to a camera (Princeton Instruments ProEM:512) measured the angle-dependent extinction. A bandpass filter (BPF, 620 nm) was incorporated when the images were measured on the Fourier plane.

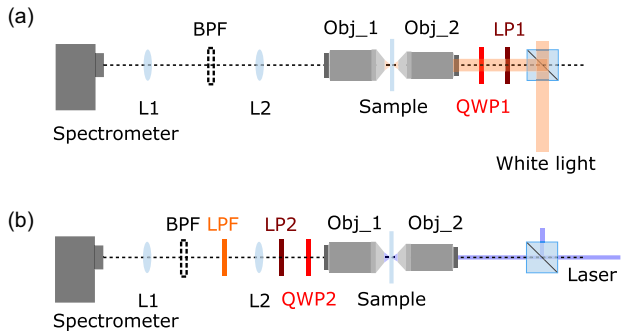

Fig. 8. (a) Schematic illustration of the Fourier setup for extinction measurements. (b) Schematic illustration of the Fourier setup for PL measurements. Obj_1 is a 60× or 100× objective lens and Obj_2 is a 40× objective lens. LP1 is a linear polarizer and QWP1 is a quarter-wave plate (Thorlabs FR600QM). LP2 is a linear polarizer and QWP2 is a quarter-wave plate (Thorlabs AQWP05M-600). LPF is a long-pass filter (550 nm). BPF is a bandpass filter (Thorlabs FBH620-10). The excitation source for the PL is a pulsed laser with a central wavelength of 400 nm.

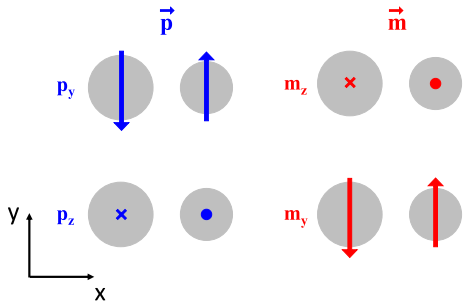

Fig. 9. Schematics of dipole orientation for p_y, p_z, m_y, and m_z modes.

3. Angle-Dependent Photoluminescence Measurements

Angle-dependent PL was measured with a modified Fourier microscope, as depicted in Fig. 8(b). The sample was illuminated with a C-Wave laser (Hübner GmbH) through a 40× objective (Nikon CFI S Plan Fluor ELWD, NA = 0.6) and collected using a 100× objective (Nikon Plan, NA = 0.9). The excitation wavelength for the PL was set at 532 nm with a power density of 0.29 W/cm^2. No additional polarizer was used for excitation and the integration time for the PL was set to 5 s. Adjusting the relative angle (±45°) between QWP2 and LP2, the right-handed and left-handed PL signals could be separated. A 550 nm long-pass filter (LPF) was used to eliminate the laser signal used for excitation. Additionally, a 620 nm BPF was introduced when capturing images of the PL signal on the Fourier plane.

4. COMSOL Multiphysics Simulations

Infinite metasurfaces as depicted in Fig. 1 are simulated with the Electromagnetic Waves in Frequency Domain module of COMSOL Multiphysics. The unit cell consists of two poly-Si disks on a SiO_2 substrate with a 300 nm thick layer of PMMA on top. The system is limited in the two vertical directions by perfectly matched layers (PMLs). The x and y limits of the unit cell are set as periodic boundary conditions to reproduce the infinite metasurface. The system is solved to obtain the eigenmodes of the electromagnetic field with $k = 0$ within the visible range. The dipole orientation of the p_y, p_z, m_y, and m_z modes are schematically shown in Fig. 9.

APPENDIX B: SYMMETRY OF THE MODES, ANALYTIC MODEL FOR THE CIRCULAR DICHROISM

This appendix presents an analytic model based on group-theoretical considerations, which describes the symmetry of the M1–M4 modes and explains the observed circular dichroism. In Fig. 10, we show a schematic of the 2D lattice and the unit cell for two cases: in Fig. 10(a) the size-detuned metasurface with point group C_{2v}, where the two pillars in the unit cell have different radii but the yz-symmetry plane is maintained, and in Fig. 10(b) the size- and position-detuned metasurface with point group C_{1v}, where the distance between the two pillars in the unit cell is modified and the mirror symmetry in the yz plane is broken. Notice that the symmetry of the whole structure does not depend on the choice of the unit cell in Fig. 10, which has only a graphic purpose, as it shows that the size-detuned lattice maintains yz mirror symmetry. The structure in Fig. 10(b) corresponds to the metasurface experimentally investigated, while the structure in Fig. 10(a) is the starting point to understand the formation of BICs and the mechanism of symmetry breaking. The structure in Fig. 10(a) supports two symmetry-protected BICs at $k = 0$ with irreducible representations (irreps) named A_1 and A_2, while the two BICs become quasi-BICs in structure of Fig. 10(b), with symmetries A' and A'', respectively.

To understand the symmetry of the photonic modes in the size-detuned metasurface, we can adopt a simple approximation and keep only plane waves with reciprocal lattice vectors $\mathbf{G} = (\pm G, 0)$, where $G = 2\pi/a_x$. In Table 2 we show the basic states at $k = 0$ and their full 3D symmetries, i.e., both under mirror reflection in the xy plane and under the

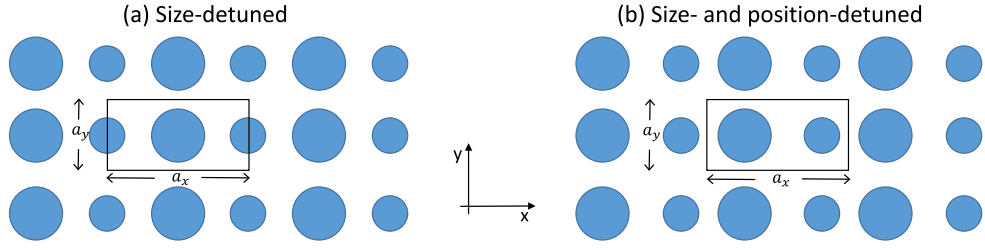

C_{2v}	E	$C_2(z)$	$\sigma_v(xz)$	$\sigma_v(yz)$	dipole
A_1	1	1	1	1	p_z (BIC)
A_2	1	1	−1	−1	m_z(BIC)
B_1	1	−1	1	−1	p_x, m_y
B_2	1	−1	−1	1	p_y, m_x

C_{1v}	E	$\sigma_v(xz)$	dipole
A'	1	1	p_x, p_z, m_y
A''	1	−1	p_y, m_x, m_z

Compatibility: $A_1, B_1 \rightarrow A'$
$A_2, B_2 \rightarrow A''$

Fig. 10. Schematic structure with unit cell, and character tables of the corresponding point group, for (a) the size-detuned structure with point group C_{2v}, supporting two BICs, and (b) the size- and position-detuned structure with point group C_{1v}. The symmetries of electric (**p**) and magnetic (**m**) dipole components are indicated. Panel (b) shows also the compatibility relations for the reduction of symmetry from C_{2v} to C_{1v}.

Table 2. Symmetry of Photonic Eigenmodes at $k = 0$ for the Size-Detuned Metasurface of Fig. 10(a)[a]

Fields	Irrep C_{2v}	Irrep C_{1v}	Mode
$\mathbf{E} = E_0\hat{y}(e^{iGx} + e^{-iGx})$ $\mathbf{H} = H_0\hat{z}(e^{iGx} - e^{-iGx})$	B_2	A''	xy-even, p_y
$\mathbf{E} = E_0\hat{y}(e^{iGx} - e^{-iGx})$ $\mathbf{H} = H_0\hat{z}(e^{iGx} + e^{-iGx})$	A_2	A''	xy-even, m_z
$\mathbf{E} = E_0\hat{z}(e^{iGx} + e^{-iGx})$ $\mathbf{H} = H_0\hat{y}(e^{iGx} - e^{-iGx})$	A_1	A'	xy-odd, p_z
$\mathbf{E} = E_0\hat{z}(e^{iGx} - e^{-iGx})$ $\mathbf{H} = H_0\hat{y}(e^{iGx} + e^{-iGx})$	B_1	A'	xy-odd, m_y

[a]The left column shows the dominant field components of the basic states. The two central columns indicate their irreducible representations in the point groups C_{2v} and C_{1v}, respectively. The right column gives the corresponding symmetry under mirror reflection in the xy plane, and the dipolar character of the mode.

operations of the 2D point group. The latter can be derived by looking at the transformation properties under the C_{2v} operations $E, C_2(z), \sigma_v(xz), \sigma_v(yz)$ and comparing with the character tables of Fig. 10. There are four modes, two of which are even with respect to reflection in the xy plane (or xy-even, sometimes called TE-like in photonic crystal terminology), and two are odd with respect to reflection in the xy plane (xy-odd, called TM-like). One of the xy-even and one of the xy-odd modes are symmetry-protected BICs at $k = 0$. This is in line with the conclusions of Ref. [49], where only xy-even states were considered.

We further analyze the circular dichroism for $k_y \neq 0$. For $\mathbf{k} = k_y\hat{y}$ along the Γ-Y direction in the symmetry-broken metasurface, there are no symmetry operations beyond the identity, thus the two xy-even modes are coupled to each other, and so are the two xy-odd modes. At $k_y \neq 0$, the system has no vertical symmetry planes, and a circular dichroism takes place in the optical response. To treat this situation, we follow the approach of Ref. [56] and calculate the far-field polarization vector $\mathbf{d}$ from a spatial average of the periodic part of the electric field $\mathbf{E_k(r)}$ in the unit cell. For a given in-plane wavevector $\mathbf{k}$, we again model the system with two plane waves $e^{i(\mathbf{k}+\mathbf{G}_j)\cdot\mathbf{r}}$, where $j = 1,2$ and $\mathbf{G}_j = (\pm G, 0)$. The in-plane projections of the polarization field are then obtained as follows:

$$xy\text{-even modes: } \mathbf{d_k} = \sum_j c_j\hat{\varepsilon}_j, \tag{B1}$$

$$xy\text{-odd modes: } \mathbf{d_k} = \sum_j c_j\hat{g}_j, \tag{B2}$$

where we define

$$\mathbf{k} + \mathbf{G} \to \mathbf{k} + \mathbf{G}_j \equiv \mathbf{g}_j, \quad \hat{g}_j = \frac{\mathbf{g}_j}{|\mathbf{g}_j|}, \tag{B3}$$

$$\hat{\varepsilon}_j = \hat{z} \times \frac{\mathbf{k} + \mathbf{G}_j}{|\mathbf{k} + \mathbf{G}_j|} = \hat{z} \times \hat{g}_j = \frac{1}{g_j}(-g_{jy}, g_{jx}). \tag{B4}$$

In the investigated metasurface, the two plane waves $e^{\pm iGx}$ are coupled unequally because of the symmetry breaking, and thus the coefficients c_1, c_2 are not simply ± 1 as for the field components in Table 2. To account for loss of yz mirror symmetry, we consider the coefficients $c_1 = e^{i\phi}$, $c_2 = \pm e^{-i\phi}$ (for xy-even modes) or $c_1 = e^{i\psi}$, $c_2 = \pm e^{-i\psi}$ (for xy-odd modes), where ϕ, ψ are symmetry-breaking parameters. It is then straightforward to calculate the polarization vector and Stokes parameters S_0, S_1, S_2, S_3. In particular, we are interested in the normalized Stokes parameter S_3/S_0, which is a measure of the circular polarization of the mode and is directly related to the circular dichroism [56,57]. We then obtain the results in Table 3, which are considered to be valid at small wavevector k_y, because of the approximation of coupling only two modes. It should be remarked that in the case of the C_{2v} symmetric lattice of Fig. 10(a), the basic modes of Table 2 are uncoupled and we must have $\phi = \psi = 0$, which implies $S_3 = 0$ and vanishing CD. Notice that in this case, only the modes with p_y and m_y symmetry are coupled to far-field radiation in the normal direction ($k_y = 0$), while the modes with p_z and m_z symmetry are uncoupled BICs. For the symmetry-broken metasurface of Fig. 10(b) instead, the results show that for the positive k_y direction there are two modes with $S_3 > 0$, and two others with $S_3 < 0$. Basically, the two coupled xy-even modes are predicted to have opposite CD, and the same for the two coupled xy-odd modes: this is in agreement with the experimental results reported in Section 3, Fig. 2(c). Moreover, S_3 is odd in k_y, and therefore the CD is predicted to change sign when reversing the angle of incidence from θ to $-\theta$. Thus, the analytic treatment accounts for the main features observed in the experiments and in the numerical simulation.

Table 3. Far-Field Polarization Vector and Normalized Stokes Parameter S_3/S_0 for the Photonic Modes Close to $k = 0$ (with $G = 2\pi/a_x$)

Symmetry	c_1	c_2	Far-Field Polarization $\mathbf{d_k}$	$\frac{S_3}{S_0}$
xy-even, p_y	$e^{i\phi}$	$-e^{i\phi}$	$-i\hat{x}k_y \sin\phi + \hat{y}G\cos\phi$	$\frac{2k_yG\sin\phi\cos\phi}{G^2\cos^2\phi+k_y^2\sin^2\phi}$
xy-even, m_z	$e^{i\phi}$	$e^{i\phi}$	$-\hat{x}k_y\cos\phi + i\hat{y}G\sin\phi$	$\frac{-2k_yG\sin\phi\cos\phi}{G^2\sin^2\phi+k_y^2\cos^2\phi}$
xy-odd, p_z	$e^{i\psi}$	$e^{i\psi}$	$i\hat{x}G\sin\psi + \hat{y}k_y\cos\psi$	$-\frac{2k_yG\cos\psi\sin\psi}{G^2\sin^2\psi+k_y^2\cos^2\psi}$
xy-odd, m_y	$e^{i\psi}$	$-e^{i\psi}$	$\hat{x}G\cos\psi + i\hat{y}k_y\sin\psi$	$\frac{2k_yG\cos\psi\sin\psi}{G^2\cos^2\psi+k_y^2\sin^2\psi}$

APPENDIX C: OPTICAL AND PHOTOLUMINESCENCE IMAGES OF SAMPLE S0

An optical image of a corner of the S0 metasurface was taken with a 20× objective (NA = 0.45) and white light illumination, as shown in Fig. 11(a). The purple region corresponds to the array, while the remaining gray region is the substrate. The PL image of the same area was imaged using an X-Cite 120 white light source with a 445 ± 15 nm bandpass filter as excitation and a 550 nm long-pass filter to remove the excitation light [Fig. 11(b)]. The emission of the dye is more intense from the region with the metasurface than that from the substrate, which can be attributed mainly to the combination of pump enhancement by the nanoparticle array at the excitation wavelengths, and the collection enhancement by the directional outcoupling of the emission by the array. To a lesser extent,

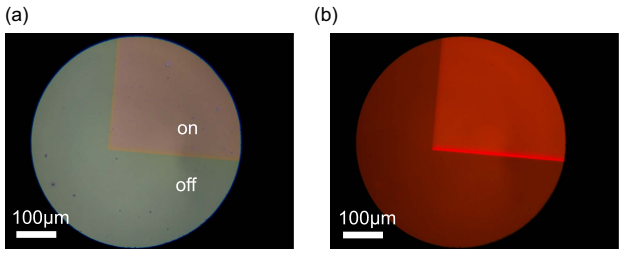

Fig. 11. Optical microscope image (a) and PL image (b) of a corner of S0 with the dye/PMMA layer on top. The off-the-array region corresponds to the dye/PMMA layer on top of the substrate.

Purcell enhancement by the modified local density of optical states can contribute to the modified emission of the dye on top of the metasurface.

APPENDIX D: DISPERSION AND ENHANCEMENT OF CPL OF SAMPLES S1–S5

Figures 12(a) and 12(b) show the angle-dependent RCPL and LCPL spectra of samples S1–S5. From S1 to S5, the lattice constant of the array increases (see Table 1), resulting in a redshift of the modes. The absolute PL intensity is related to the metasurface and the dye. To investigate the role of the metasurface in the enhancement of emission, the PL dispersions of S1–S5 are normalized by the dispersion measured on the flat PMMA/dye surface (without the metasurface). Figures 12(c) and 12(d) illustrate the angle-dependent PL enhancement. In the plots of the PL intensity, the maximum value is around 2 eV, which corresponds to the excitonic transition of the dye. The maximum PL enhancement determined by metasurface is approximately 13 times and occurs at $k_y \simeq \pm 3.5$ rad/μm for S5.

APPENDIX E: SIMULATIONS OF DIRECTIONALITY IN EMISSION

Figures 13(a)–13(e) show a simulation of the directional emission intensities previously discussed in Fig. 7. The curves are obtained by calculating the absorption, which is the reciprocal process of emission and is proportional to the PL intensity, at a fixed wavelength (the relation between absorption and emission couplings is embodied, e.g., in temporal coupled-mode theory [58,59]). We consider the metasurface coated with PMMA/dye, whose refractive index is $n = 1.59$. We choose a wavelength $\lambda = 620$ nm ($E = 2$ eV), for metasurface parameters that represent the trend of increasing lattice constant for samples S1 to S5, as in Table 1. Figure 13(a) refers to the case when the energy $E = 2$ eV lies just below the lowest photonic mode at $k_y = 0$; see left panels in Fig. 12. Then the emission intensity is broad in the angle, with a peak around k_y that is the precursor of the photonic mode at slightly higher energy. With increasing lattice constant, the bands are redshifted and become resonant with the selected energy, producing narrow directional emission peaks. The emission directions change with the lattice constant and more emission peaks appear as more photonic modes cross the selected energy. These features are similar to the measured directional emission in Fig. 7, although the experimental peaks are broader due to the spectral window $\lambda = 620 \pm 10$ nm. The simulations validate the interpretation of the directional

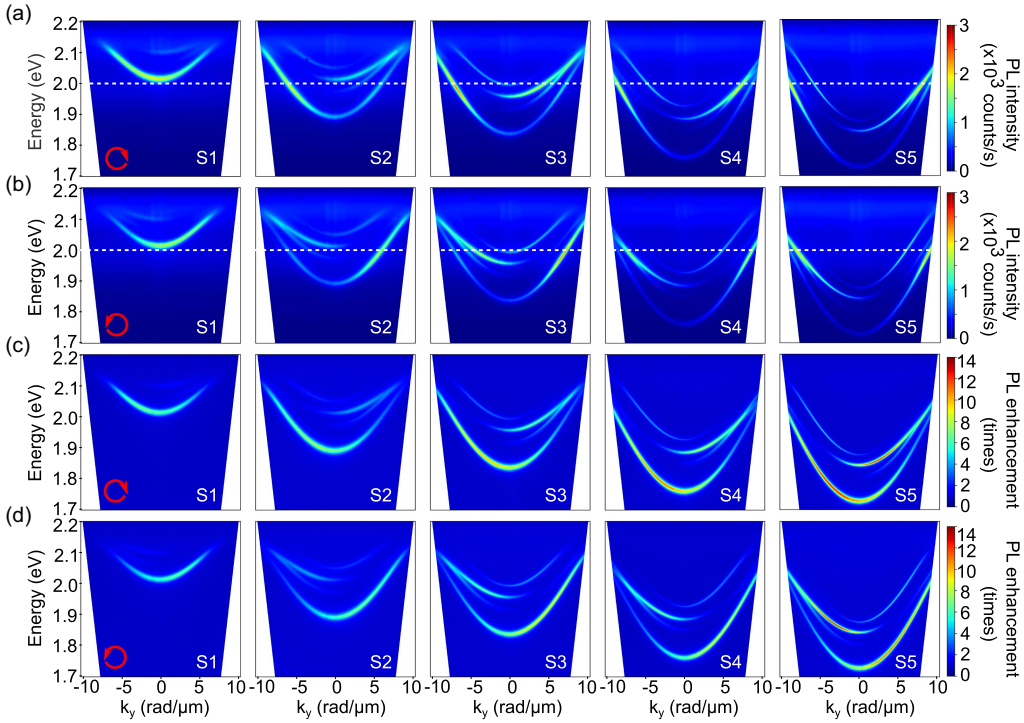

Fig. 12. Experimental dispersion of the RCPL (a), LCPL (b), RCPL enhancement (c), and LCPL enhancement (d) from the PMMA/dye films on samples S1 to S5. The horizontal white dashed lines in (a) and (b) indicate the center wavelength position of the bandpass filter (FBH620-10, Thorlabs) used for the measurements shown in Fig. 7.

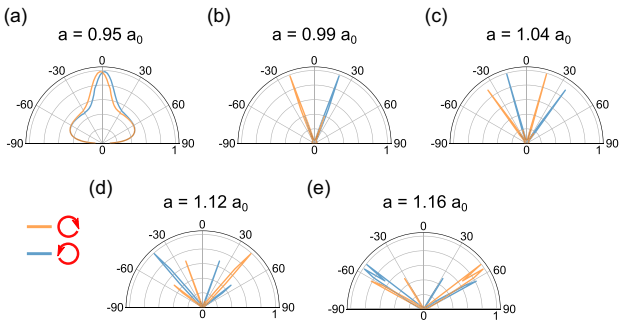

Fig. 13. Simulated intensities for RCPL (orange curves) and LCPL (blue curves) at a wavelength of 620 nm as a function of the angle along y for metasurfaces that represent the trends of samples S1–S5, like in Fig. 7. They are obtained from sample S0 by scaling the 2D parameters (d, L, and a) with scale factors $s = 0.95$ (a), $s = 0.99$ (b), $s = 1.04$ (c), $s = 1.12$ (d), and $s = 1.16$ (e).

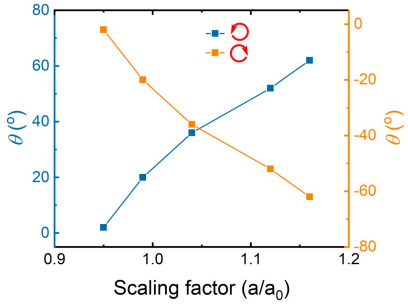

Fig. 14. Simulated angles of the photonic mode M4 (p_y) as a function of the scaling factor. The data are extracted from Fig. 13. The orange and blue curves represent RCPL and LCPL, respectively. The wavelength is fixed at 620 nm.

emission measurements in Fig. 7. They confirm that the directional chiral emission is intrinsically very narrow and can be controlled by the lattice constant. To further demonstrate the relationship between emission angles and scaling factor, the data of a representative mode (M4) in Fig. 13 were extracted and plotted in Fig. 14. Along with the increase of scaling factor, the angles (normal as reference) of LCPL and RCPL also increase. The angles can be tuned from 2° to 62° within a scaling factor range from 0.95 to 1.16, which shows a large degree of tunability for the emission angles.

Acknowledgment. Funded by the European Union (SCOLED Grant Agreement Number 101098813). Views and opinions expressed are, however, those of the author(s) only and do not necessarily reflect those of the European Union or the European Innovation Council and SMEs Executive Agency (EISMEA). Neither the European Union nor the granting authority can be held responsible for them. Funded by the Dutch Organization for Scientific Research (NWO) through the Gravitation Grant Research Centre for Integrated Nanophotonics. LCA acknowledges financial support from Italian MUR through PNRR project PE0000023-NQSTI. JASG and JLP acknowledge financial support from Spanish Ministerio de Ciencia, Innovación y Universidades and Agencia Estatal de Investigación (MCIN/AEI/10.13039/501100011033), ERDF A way of making Europe, and NextGenerationEU/PRTR (PID2022-137569NB-C41, TED2021-131417B-I00, TED2021-130786B-I00, PID2021-126046OB-C22, PID2020-113533RB-C33, and PRTR-C17.I1). JLP also acknowledges the financial support from NextGenerationEU (CONVREC-2021-23). SM acknowledges financial support from the Bilateral Joint Research Project (JPJSBP120239921) from Japan Society for the Promotion of Science. HD acknowledges financial support from the China Scholarship Council (CSC202206320284).

Disclosures. The authors declare no conflicts of interest.

Data Availability. Data underlying the results presented in this paper are not publicly available at this time but may be obtained from the authors upon reasonable request.

REFERENCES

1. W. T. B. Kelvin, *The Molecular Tactics of a Crystal* (Clarendon, 1894).
2. E. Petronijevic, E. M. Sandoval, M. Ramezani, *et al.*, "Extended chiro-optical near-field response of achiral plasmonic lattices," J. Phys. Chem. C **123**, 23620–23627 (2019).
3. E. S. A. Goerlitzer, R. Mohammadi, S. Nechayev, *et al.*, "Chiral surface lattice resonances," Adv. Mater. **32**, 2001330 (2020).
4. S. Zhao, L. Shao, J. Wang, *et al.*, "Chirality-selective transparency induced by lattice resonance in bilayer metasurfaces," Photonics Res. **9**, 484–493 (2021).
5. E. Petronijevic, A. Belardini, T. Cesca, *et al.*, "Rich near-infrared chiral behavior in diffractive metasurfaces," Phys. Rev. Appl. **16**, 014003 (2021).
6. A. Movsesyan, L. V. Besteiro, X.-T. Kong, *et al.*, "Engineering strongly chiral plasmonic lattices with achiral unit cells for sensing and photodetection," Adv. Opt. Mater. **10**, 2101943 (2022).
7. S. Qiao, Q. Liang, X. Zhang, *et al.*, "Flexible engineering of circular dichroism enabled by chiral surface lattice resonances," APL Photonics **7**, 116104 (2022).
8. E. S. A. Goerlitzer, M. Zapata-Herrera, E. Ponomareva, *et al.*, "Molecular-induced chirality transfer to plasmonic lattice modes," ACS Photonics **10**, 1821–1831 (2023).
9. A. M. Romashkina, V. B. Novikov, and T. V. Murzina, "Collective lattice and plasmonic resonances in the enhancement of circular dichroism in disk-rod metasurface," J. Appl. Phys. **133**, 043103 (2023).
10. Q. Ling, Q. Liang, X. Zhang, *et al.*, "Toroidal electric dipole enabled chiral surface lattice resonances in stereo propeller metasurfaces," APL Photonics **8**, 086114 (2023).
11. L. Cerdán, L. Zundel, and A. Manjavacas, "Chiral lattice resonances in 2.5-dimensional periodic arrays with achiral unit cells," ACS Photonics **10**, 1925–1935 (2023).
12. X. Luo, X. Du, R. Huang, *et al.*, "High-Q and strong chiroptical responses in planar metasurfaces empowered by Mie surface lattice resonances," Laser Photonics Rev. **17**, 2300186 (2023).
13. M. Manoccio, V. Tasco, F. Todisco, *et al.*, "Surface lattice resonances in 3D chiral metacrystals for plasmonic sensing," Adv. Sci. **10**, 2206930 (2023).
14. M. Cotrufo, C. I. Osorio, and A. F. Koenderink, "Spin-dependent emission from arrays of planar chiral nanoantennas due to lattice and localized plasmon resonances," ACS Nano **10**, 3389–3397 (2016).
15. M. Hentschel, M. Schäferling, X. Duan, *et al.*, "Chiral plasmonics," Sci. Adv. **3**, e1602735 (2017).
16. C. Yan, X. Wang, T. V. Raziman, *et al.*, "Twisting fluorescence through extrinsic chiral antennas," Nano Lett. **17**, 2265–2272 (2017).
17. K. Q. Le, S. Hashiyada, M. Kondo, *et al.*, "Circularly polarized photoluminescence from achiral dye molecules induced by plasmonic

two-dimensional chiral nanostructures," J. Phys. Chem. C **122**, 24924–24932 (2018).
18. P. Pachidis, B. M. Cote, and V. E. Ferry, "Tuning the polarization and directionality of photoluminescence of achiral quantum dot films with chiral nanorod dimer arrays: Implications for luminescent applications," ACS Appl. Nano Mater. **2**, 5681–5687 (2019).
19. I. C. Seo, Y. Lim, S.-C. An, *et al.*, "Circularly polarized emission from organic-inorganic hybrid perovskites via chiral Fano resonances," ACS Nano **15**, 13781–13793 (2021).
20. Y. Chen, W. Du, Q. Zhang, *et al.*, "Multidimensional nanoscopic chiroptics," Nat. Rev. Phys. **4**, 113–124 (2021).
21. H. Ali, E. Petronijevic, G. Pellegrini, *et al.*, "Circular dichroism in a plasmonic array of elliptical nanoholes with square lattice," Opt. Express **31**, 14196–14211 (2023).
22. Y. Sun, Z. Hu, K. Shi, *et al.*, "Enhancing circularly polarized emission by a planar chiral dielectric metasurface," Adv. Opt. Mater. **11**, 2300197 (2023).
23. M. Ramamurthy, P. Pachidis, B. M. Cote, *et al.*, "Circularly polarized photoluminescence from nanostructured arrays of light emitters," ACS Appl. Opt. Mater. **1**, 491–499 (2023).
24. C. W. Hsu, B. Zhen, A. D. Stone, *et al.*, "Bound states in the continuum," Nat. Rev. Mater. **1**, 16048 (2016).
25. S. I. Azzam and A. V. Kildishev, "Photonic bound states in the continuum: from basics to applications," Adv. Opt. Mater. **9**, 2001469 (2021).
26. M. Kang, T. Liu, C. Chan, *et al.*, "Applications of bound states in the continuum in photonics," Nat. Rev. Phys. **5**, 659–678 (2023).
27. K. Koshelev, S. Lepeshov, M. Liu, *et al.*, "Asymmetric metasurfaces with high-*Q* resonances governed by bound states in the continuum," Phys. Rev. Lett. **121**, 193903 (2018).
28. A. Kodigala, T. Lepetit, Q. Gu, *et al.*, "Lasing action from photonic bound states in continuum," Nature **541**, 196–199 (2017).
29. M.-S. Hwang, K.-Y. Jeong, J.-P. So, *et al.*, "Nanophotonic nonlinear and laser devices exploiting bound states in the continuum," Commun. Phys. **5**, 106 (2022).
30. A. Tittl, A. Leitis, M. Liu, *et al.*, "Imaging-based molecular barcoding with pixelated dielectric metasurfaces," Science **360**, 1105–1109 (2018).
31. A. Overvig, N. Yu, and A. Alù, "Chiral quasi-bound states in the continuum," Phys. Rev. Lett. **126**, 073001 (2021).
32. K.-H. Kim and J.-R. Kim, "High-*Q* chiroptical resonances by quasi-bound states in the continuum in dielectric metasurfaces with simultaneously broken in-plane inversion and mirror symmetries," Adv. Opt. Mater. **9**, 2101162 (2021).
33. Y. Chen, H. Deng, X. Sha, *et al.*, "Observation of intrinsic chiral bound states in the continuum," Nature **613**, 474–478 (2023).
34. L. Kühner, F. J. Wendisch, A. A. Antonov, *et al.*, "Unlocking the out-of-plane dimension for photonic bound states in the continuum to achieve maximum optical chirality," Light Sci. Appl. **12**, 250 (2023).
35. T. Shi, Z.-L. Deng, G. Geng, *et al.*, "Planar chiral metasurfaces with maximal and tunable chiroptical response driven by bound states in the continuum," Nat. Commun. **13**, 4111 (2022).
36. J. Wu, X. Xu, X. Su, *et al.*, "Observation of giant extrinsic chirality empowered by quasi-bound states in the continuum," Phys. Rev. Appl. **16**, 064018 (2021).
37. W. Liu, B. Wang, Y. Zhang, *et al.*, "Circularly polarized states spawning from bound states in the continuum," Phys. Rev. Lett. **123**, 116104 (2019).
38. M. V. Gorkunov, A. A. Antonov, and Y. S. Kivshar, "Metasurfaces with maximum chirality empowered by bound states in the continuum," Phys. Rev. Lett. **125**, 093903 (2020).
39. K. Koshelev, Y. Tang, Z. Hu, *et al.*, "Resonant chiral effects in nonlinear dielectric metasurfaces," ACS Photonics **10**, 298–306 (2023).
40. X. Zhang, Y. Liu, J. Han, *et al.*, "Chiral emission from resonant metasurfaces," Science **377**, 1215–1218 (2022).
41. Y. Lim, I. C. Seo, S. An, *et al.*, "Maximally chiral emission via chiral quasibound states in the continuum," Laser Photonics Rev. **17**, 2200611 (2022).
42. S. Kim, S.-C. An, Y. Kim, *et al.*, "Chiral electroluminescence from thin-film perovskite metacavities," Sci. Adv. **9**, eadh0414 (2023).
43. G. Lozano, D. J. Louwers, S. R. Rodríguez, *et al.*, "Plasmonics for solid-state lighting: enhanced excitation and directional emission of highly efficient light sources," Light Sci. Appl. **2**, e66 (2013).
44. I. Staude, A. E. Miroshnichenko, M. Decker, *et al.*, "Tailoring directional scattering through magnetic and electric resonances in subwavelength silicon nanodisks," ACS Nano **7**, 7824–7832 (2013).
45. Y. H. Fu, A. I. Kuznetsov, A. E. Miroshnichenko, *et al.*, "Directional visible light scattering by silicon nanoparticles," Nat. Commun. **4**, 1527 (2013).
46. S. Wang, Q. Le-Van, T. Peyronel, *et al.*, "Plasmonic nanoantenna arrays as efficient etendue reducers for optical detection," ACS Photonics **5**, 2478–2485 (2018).
47. M. S. Abdelkhalik, A. Vaskin, T. López, *et al.*, "Surface lattice resonances for beaming and outcoupling green μLEDs emission," Nanophotonics **12**, 3553–3562 (2023).
48. Y. Mohtashami, L. K. Heki, M. S. Wong, *et al.*, "Metasurface light-emitting diodes with directional and focused emission," Nano Lett. **23**, 10505–10511 (2023).
49. S. Murai, D. R. Abujetas, L. Liu, *et al.*, "Engineering bound states in the continuum at telecom wavelengths with non-Bravais lattices," Laser Photonics Rev. **16**, 2100661 (2022).
50. K. B. Dossou, L. C. Botten, A. A. Asatryan, *et al.*, "Modal formulation for diffraction by absorbing photonic crystal slabs," J. Opt. Soc. Am. A **29**, 817–831 (2012).
51. B. Sturmberg, K. Dossou, F. P. R. McPhedran, *et al.*, "Emustack: an open source route to insightful electromagnetic computation via the Bloch mode scattering matrix method," Comput. Phys. Commun. **202**, 276–286 (2016).
52. E. Palik, *Handbook of Optical Constants of Solids* (Elsevier, 1997).
53. L. C. Andreani and D. Gerace, "Photonic-crystal slabs with a triangular lattice of triangular holes investigated using a guided-mode expansion method," Phys. Rev. B **73**, 235114 (2006).
54. M. Minkov, I. A. D. Williamson, L. C. Andreani, *et al.*, "Inverse design of photonic crystals through automatic differentiation," ACS Photonics **7**, 1729–1741 (2020).
55. S. Zanotti, M. Minkov, D. Nigro, *et al.*, "Legume: a free implementation of the guided-mode expansion method for photonic crystal slabs," Comput. Phys. Commun. **304**, 109286 (2024).
56. L. Zagaglia, S. Zanotti, M. Minkov, *et al.*, "Polarization states and far-field optical properties in dielectric photonic crystal slabs," Opt. Lett. **48**, 5017–5020 (2023).
57. W. Chen, Q. Yang, Y. Chen, *et al.*, "Extremize optical chiralities through polarization singularities," Phys. Rev. Lett. **126**, 253901 (2021).
58. S. Fan, W. Suh, and J. D. Joannopoulos, "Temporal coupled-mode theory for the fano resonance in optical resonators," J. Opt. Soc. Am. A **20**, 569–572 (2003).
59. W. Suh, Z. Wang, and S. Fan, "Temporal coupled-mode theory and the presence of non-orthogonal modes in lossless multimode cavities," IEEE J. Quantum Electron. **40**, 1511–1518 (2004).